Journal of Nondestructive Evaluation, Vol. 22, No. 2, June 2003 (© 2003)

Rayleigh Wave Propagation for the Detection of Near Surface Discontinuities: Finite Element Modeling

A. Zerwer,[1] M. A. Polak,[2,4] and J. C. Santamarina[3]

Received 9/11/00; Revised 6/23/03

The paper presents a finite element study designed to gain physical insight into the effect of surface discontinuities on Rayleigh wave propagation in structural elements. In particular, a series of array measurements at various locations within a plate are simulated and compared with experimental measurements. Conversion of array measurements into the frequency-wavenumber domain reveals propagating Lamb modes, which are used to define Rayleigh wave motion. Numerical results show that Rayleigh waves measured after passing a fracture are composed of long wavelength Rayleigh wave energy propagating past the slot and short wavelength Rayleigh wave energy formed behind the slot.

KEY WORDS: Rayleigh waves; Lamb waves; finite elements; defect dimension; mode shapes; plates.

1. INTRODUCTION

Cracks denounce the type and magnitude of loads (present or past), and define the integrity of structural members. Therefore proper assessment of cracks is needed for decisions regarding rehabilitation, strengthening, and rebuilding of existing structures. Transillumination tomographic techniques can reveal internal defects; however, their reduced information content near free surfaces restricts their ability to detect surface features such as flaws and cracks. Conversely, Rayleigh waves are particularly wellsuited for free surface condition assessment: they propagate along free surfaces, they involve the majority of the energy of the propagating wave modes, they experience lower spatial attenuation, and the depth assessed by surface waves can be controlled by changing the frequency. Therefore understanding the physical interaction between the propagating Rayleigh wave and surface fractures is very important and can lead to better nondestructive techniques for crack detection.

A variety of Rayleigh wave–based testing methods have been proposed for the detection of surface fractures. The methods can be categorized depending on the ratio of the incident wavelength (λ) to the crack depth (d). When the ratio $\lambda/d << 1$, reflections are used to locate a crack and reflection amplitudes are used to determine crack depth.[1–5] As the wavelength approaches the crack depth ($\lambda/d \approx 1$) resonance methods are employed. Oscillations or resonances observed in measured transmission and reflection coefficients provide estimates of crack depth and width.[6–9] Spectral methods are typically used when the wavelengths are significantly larger than the crack depth ($\lambda/d << 1$). Power spectral measurements of transmitted Rayleigh

[1] Geotechnical Specialist, Trow Consulting Engineers, Sudbury, Ontario, Canada.
[2] Associate Professor, Department of Civil Engineering, University of Waterloo, Ontario, Canada.
[3] Professor, Department of Civil and Environmental Engineering, Georgia Institute of Technology, Atlanta, Georgia.
[4] Corresponding author: E-mail: polak@uwaterloo.ca

waves reveal changes in spectral amplitude for different crack depths.[5,10] Finally, the spectral analysis of surface waves (SASW) uses a broadband spectrum to detect changes in phase velocity with depth for a broad range of λ/d ratios.[11,12]

The detection and sizing of cracks using Rayleigh waves remains challenging, in part because of the complex phenomenology related to Rayleigh wave–fracture interaction. The work presented in this paper was done as part of a research program on Rayleigh wave propagation for the assessment of structural elements.[13] The aim of this research program was to develop a nondestructive testing methodology for the detection of surface cracks and the definition of their location and size. The research program consisted of both experimental and numerical components. The experimental work was documented in Zerwer *et al.*[14–16], in which testing methodology and signal processing were described.

The numerical work is documented herein. The study is implemented with a commercially available finite element package, ABAQUS. The paper begins with a brief presentation of Lamb wave propagation in plates to set the basis for data interpretation. Then the finite element model is created to correspond to the experimental specimens and setup. Parameters for the finite element model are gathered from the literature and the authors' experimental results. The numerical study includes three sets of simulations: without a slot and with slots of two different depths. Nodal acceleration time histories at the surface of the simulated specimens provide information equivalent to a receiver array mounted at similar locations to monitor Rayleigh wave propagation within the test plate. The numerically calculated surface accelerations are compared with the previously published experimental results. Emphasis in signal analysis is placed on the frequency domain to identify the Lamb modes, which are the fundamental components of Rayleigh waves in plates. Finally, simulation results are examined to gain further insight into the Rayleigh wave–fracture interaction.

The experimental configuration modeled with finite elements consists of a thin Plexiglas plate ($1219 \times 305 \times 6$ mm^3) in an upright position. The experimental approach is to model the geometry of a typical beam or column by using a thin plate to represent a "slice" of a rectangular member (Fig. 1). In this way, two-dimensional wave propagation (generalized plane stress condition) prevails in a plate held in an upright position. The source for these measurements is a 4.74-mm (3/16″) steel bearing, dropped onto the edge of a Plexiglas sheet at a distance of 304.8 mm (12″) in front of the slot. An accelerometer coupled to the plate measures the vertical component of acceleration at different locations on the Plexiglas sheet at 41 discrete locations. The first measurement is located 25.4 mm (1″) behind the slot. Initial measurements are completed without a slot, and in subsequent measurements, the slot depth is increased at 25.4 mm (1″) intervals, up to 152.4 mm (6″).

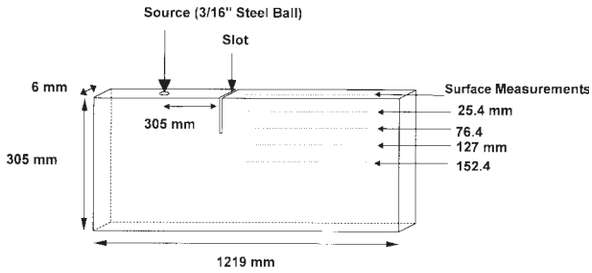

Fig. 1. Experimental configuration modeled using finite elements.

It is important to note that although experiments allow monitoring of wave propagation on surfaces only, finite element simulation results provide vibration details at all points within the body. Thus numerical results provide the analyst unparalleled insight to gain proper physical understanding of the dynamic response associated to Rayleigh wave propagation in the presence of a surface fracture. In turn, this information can guide further developments in experimental methodologies and signal analysis.

2. RAYLEIGH AND LAMB WAVES IN PLATES

The theory of wave propagation in plates is reviewed to illustrate the difference between Rayleigh and Lamb wave motions. These concepts guide data interpretation in the following section.

2.1. Dispersion Curves

Wave propagation in thin plates was first studied by Rayleigh[17] and Lamb.[18] The fundamental premise underlying the derivation of the Rayleigh-Lamb frequency equations is the interaction of compression and shear waves with two parallel traction free surfaces. The frequency equation is a transcendental function that fully describes wave motion in plates, including classical flexural plate motion, Rayleigh wave motion, and Lamb wave motion. The Rayleigh-Lamb frequency equations are

$$\frac{\tan \beta b}{\tan \alpha b} + \left\{ \frac{4\alpha\beta k^2}{\left(k^2 - \beta^2\right)^2} \right\}^{\pm 1} = 0 \qquad (1)$$

such that $\alpha^2 = \frac{\omega^2}{V_P^2} - k^2 \quad \beta^2 = \frac{\omega^2}{V_S^2} - k^2$

where b is half the plate thickness, ω is the circular frequency, k is the wavenumber, V_P is the compression wave velocity, and V_s is the shear wave velocity. Changing the exponent to either +1 or –1 provides solutions to symmetric or antisymmetric modes respectively.

The concept of generalized plane stress allows Eq. (1) to be used for thin plates, where the thickness is less than 1/10 the shortest propagating wavelength,[19] However, for generalized plane stress, Eq. 1 requires the compression wave velocity to be equal to:

$$V_P^{\text{plate}} = \sqrt{\frac{E}{\rho\left(1 - \nu^2\right)}} \qquad (2)$$

where E is Young's modulus, p is the mass density, and v is Poisson's ratio.

2.2. Mode Shapes

Dispersion curves of each Lamb mode are calculated using the Rayleigh-Lamb frequency equations (Eq. 1) to compute the mode shapes. For symmetric modes, the horizontal and the vertical displacements are given by Graff.[20]

$$u = i\left(kB\cos \alpha z + \beta C \cos \beta z\right) e^{i(kx - \omega t)} \qquad (3)$$

$$w = \left(-\alpha B \sin \alpha z + kC \sin \beta z\right) e^{i(kx - \omega t)} \qquad (4)$$

given that $\frac{B}{C} = -\frac{2k\beta \cos \beta b}{\left(k^2 - \beta^2\right)\cos \alpha b}$

where z is depth within the cross-section and B and C are constants. For antisymmetric modes the horizontal and vertical displacements are given by the following relations:

$$u = i\left(kA \sin \alpha z + \beta D \sin \beta z\right) e^{i(kx - \omega t)} \qquad (5)$$

$$w = \left(\alpha A \cos \alpha z + kD \cos \beta z\right) e^{i(kx - \omega t)} \qquad (6)$$

where A and D are arbitrary constants that satisfy:

$$\frac{A}{D} = \frac{2k\beta \sin \beta b}{\left(k^2 - \beta^2\right)\sin \alpha b}$$

Examples of the first three symmetric and antisymmetric mode shapes are shown in Figure 2. Calculations for this figure use body wave velocities for a Plexiglas plate (V_p = 2362 m/s and V_s = 1372 m/s), a thickness of b = 0.1524 m, and a wavenumber of k = 20.92 rad/m. Also shown in Figure 2 is the disappearance of the horizontal symmetric displacement at the plate surfaces, which is unique to this combination of plate thickness and wavenumber.

Mode shapes provide a basis for defining Rayleigh wave motion in plates. As shown in Figure 3, the superposition of a fundamental symmetric mode and a fundamental antisymmetric mode generates a Rayleigh wave.[6] Body wave velocities and plate thickness used to calculate the mode shapes in Figure 2 are used to determine the fundamental mode shapes in Figure 3, however, at a higher frequency of 20 kHz. At short wavelengths the phase velocities of the fundamental modes asymptotically approach the Rayleigh wave velocity.

The mode shapes in Figure 2 show that different Lamb modes have maximum amplitudes (and nodes) at dissimilar depths. Therefore the detection of a particular Lamb mode depends on the particle motion for that mode at the observation depth. Note that the horizontal motion of all antisymmetric modes is zero at half the plate thickness.

3. NUMERICAL MODEL

A finite element model is designed to explore the interrelationship between the formation of a Rayleigh wave and the corresponding Lamb modes that can exist within a plate. This relationship is studied by comparing waves propagating in a plate with and without a slot. A finite element model provides a unique opportunity to investigate Rayleigh and Lamb wave motion at various locations within a plate, phenomena that are not easily studied using experimental methods.

Finite element modeling of wave propagation problems using finite elements requires proper mesh size and time increment in view of the frequencies and wavelengths of interest. Furthermore, boundary conditions and material properties must realistically represent the experimental situation. The design of the following model pertains to simulating Rayleigh wave propagation in a thin Plexiglas plate, which was tested by the authors as part of this research program.

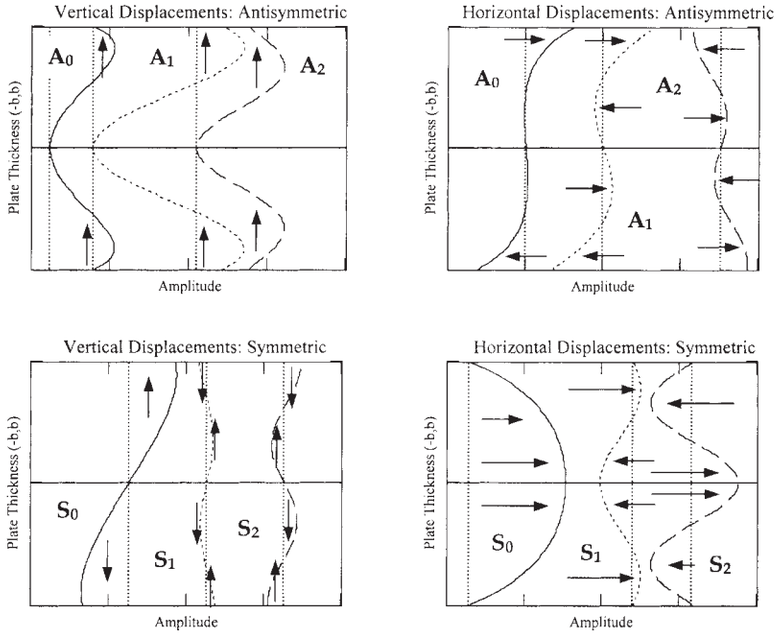

Fig. 2. Mode shapes of first two symmetric and antisymmetric modes.

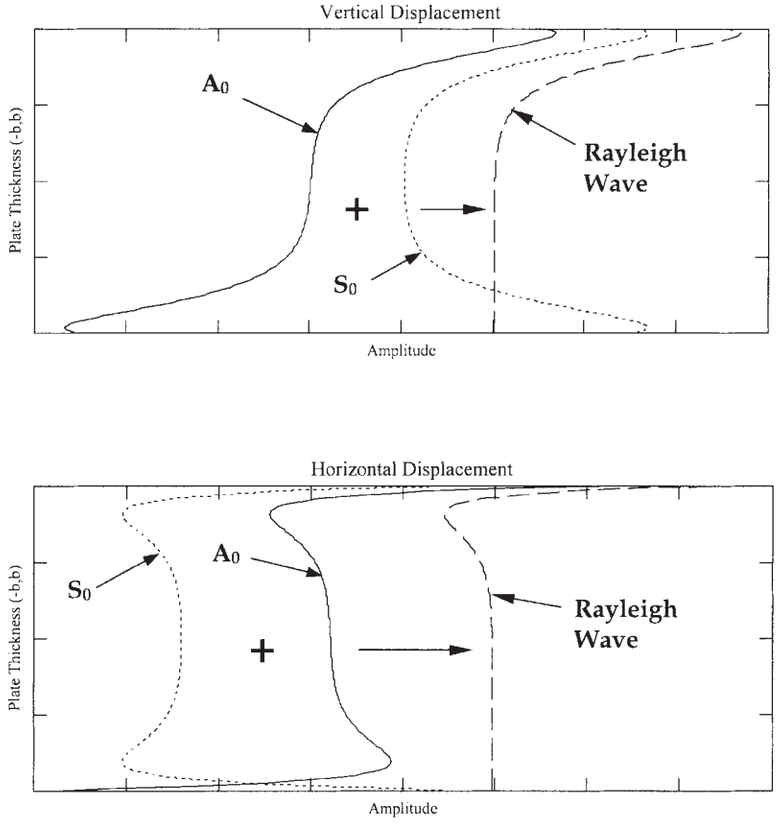

Fig. 3. The superposition of fundamental symmetric and antisymmetric modes generate a Rayleigh wave calculated at a frequency of 20 kHz and $b = 0.15$ m.

3.1. Finite Element Mesh

In wave propagation simulations, the dimension of finite elements must be selected taking into consideration the wavelength of the propagating perturbation. The mesh is a low-pass filter, therefore; large element dimensions filter short wavelengths. On the other hand, very small elements cause numerical instability. Valliappan and Murti[21] provide the following relation for estimating element size (g):

$$g \leq \varsigma \lambda_{\min} = \varsigma \frac{V_S}{f_{\max}} \tag{7}$$

The constant ς depends on whether the mass matrices are consistent ($\varsigma = 0.25$) or lumped ($\varsigma = 0.2$). The minimum wavelength ($\lambda_{\min}$) is calculated using the maximum frequency of the Rayleigh wave ($f_{\max}$) and the shear wave velocity (V_s). The highest Rayleigh wave frequency component measured in the Plexiglas experiments is $f_{\max} = 30$ kHz. For a shear wave velocity, $V_s = 1370$ m/s, the minimum wavelength is $\lambda_{\min} = 46$ mm. All simulations use a consistent mass approach for which Valliappan and Murti[21] suggest a value of $\varsigma = 0.25$. The resulting element dimension is 11.5 mm. To maintain parallelism with the array measurements, the element dimensions are increased to 12.7×12.7 mm^2. Hence, the plate is discretized into 2325 bilinear quadrilateral plane stress elements with 2425 nodes, as shown in Figure 4. A narrow set of elements with dimensions of 3×12.7 mm^2 are included in the mesh to represent the slot.

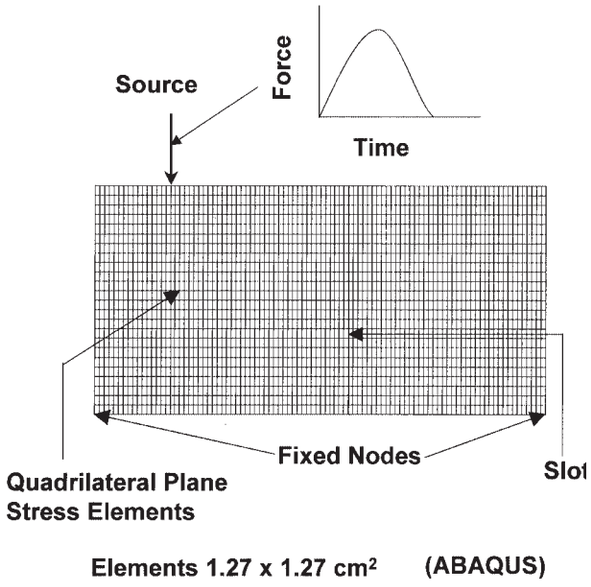

Fig. 4. Finite element model mesh design.

3.2. Time Increment

The time step is chosen with respect to the characteristic time (τ), calculated using the following equation[21]:

$$\tau \leq \frac{g}{V_P} \tag{8}$$

where g is the element dimension from Eq. (7), and V_P is the compression wave velocity. The previously selected element size dicates the time increment for the implicit solution method. For $g = 12.7$ mm and a compression wave velocity of $V_P = 2360$ m/s (Eq. 2), the characteristic time becomes $\tau = 5.38$ μs. To facilitate comparison with experimental measurements, the time increment is set to 1 μs.

3.3. Boundary Conditions

The bottom left and bottom right corner nodes of the finite element model are fixed in both the vertical and horizontal directions to properly represent the experimental configuration.

3.4. Material Properties

The simulated material is Plexiglas (polymethylmethacrylate [PMMA]). Plexiglas has viscoelastic properties; therefore elastic constants vary with frequency. For example, the elastic constants of Plexiglas between 2 and 30 kHz show that Poisson's ratio is about $\nu = 0.33$, Young's modulus varies from $E = 4.8$ GPa at 2 kHz, to 5.3 GPa at 10 kHz, and the shear modulus increases from $G = 1.8$ GPa at 2 kHz to 2.2 GPa at 10 kHz.[22] The finite element model in this study considers a linear isotropic medium with average material parameters within the suggested frequency range. Material properties are selected during preliminary numerical simulations to match numerical results with experimental measurements, rendering Young's modulus $E = 6.0$ GPa and Poisson's ratio $\nu = 0.33$. The elastic properties of the elements in the slot are set close to zero.

This is an approximate approach to modeling material behavior, and, as a consequence, the resulting finite element model can be confidently used only for the analysis of test specimens on which it is calibrated.

However, because the goal of this work is to study internal wave propagation in the specimens, the approach is valid and rational. It should be added that a more detailed approach (e.g., viscoelastic modeling of material) would enormously add to the complexity of the numerical analyses (possibly rendering the whole analysis not feasible), and it would not necessarily add to the information sought in this work on internal wave propagation. Therefore, as a compromise between accuracy and simplicity, it was decided to use a linear elastic model with calibrated material constants.

3.5. Attenuation

ABAQUS incorporates damping using a Rayleigh damping model[22]:

$$[C] = \eta_1 [M] + \eta_2 [K] \tag{9}$$

where $[C]$ is the damping matrix, $[M]$ is the mass matrix, $[K]$ is the stiffness matrix, and η_1 and η_2 are arbitrary constants. Experimental damping measurements are related to the Rayleigh damping model through the following relationship:

$$D = \frac{\eta_1}{2\omega} + \frac{\eta_2 \omega}{2} \tag{10}$$

where D is the damping ratio and ω is the circular frequency. The damping ratio measured by Koppelmann[23] ranges from $D = 0.025$ at 2 kHz to 0.015 at 10 kHz. For simulation purposes the first term on the right hand side of Eqns. (9) and (10) (mass damping) is set to zero because high damping is not measured at low frequencies. The best fit for η_2 is 1×10^{-6}, which converts to a damping ratio of $D = 0.04$.

3.6. Impact Simulation

A half-sine function is an accepted approximation for the impact of a steel ball bearing onto a flat surface.[24,25] Numerical calculations predict a 59-μs impact duration for a 4.76-mm steel ball bearing dropped from a height of 50 mm onto a medium with the stiffness of Plexiglas.[26]

4. MODEL VERIFICATION

The finite element model is verified by comparing time domain traces of nodal accelerations of surface elements obtained from the finite element model to accelerometer measurements completed on the Plexiglas plate without a slot.[14,16] Figure 5 compares finite element time domain traces with experimental measurements at three different locations along the receiver array. The main pulse of the Rayleigh wave is modeled relatively accurately, with reduced high-frequency components near the beginning of the Rayleigh wave pulse. The first arrival is the S_o (fundamental symmetric) mode.

5. ARRAY SIGNAL PROCESSING

An array of receiver measurements records Rayleigh wave propagation in complementary experi-

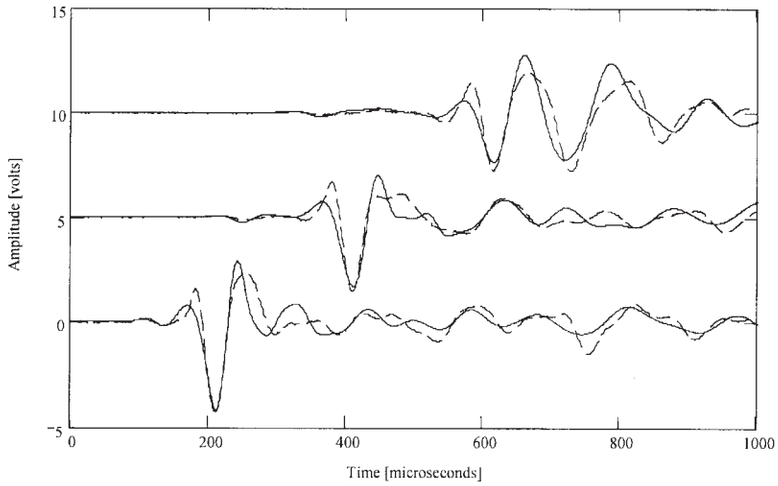

Fig. 5. Time domain traces obtained from finite element simulation compared to experimental measurements.

mental studies completed on a Plexiglas plate.[14,16] Time history measurements are stored as rows in a matrix; hence, columns designate spatial fluctuations. The two-dimensional Fourier transform converts the matrix of signals from the temporal-spatial space into the frequency-wavenumber representation. A contour plot of magnitude values calculated for each element in the transformed matrix shows a series of peaks. Each peak permits computing the phase velocity of a particular mode.[27,28]

In the corresponding finite element models, time accelerations at 41 nodes, equally spaced at 1.27 cm ($^1/_2$″), are stored in the matrix of signals. Each column contains 1000 data points sampled at 1 MHz. Figure 6 is shows a typical frequency-wavenumber plot corresponding to a finite element simulation of wave propagation in the Plexiglas plate without a slot. Main peaks indicate the presence of a Rayleigh wave. In addition to displaying dispersion, the frequency-wavenumber domain can reveal the direction of energy propagation. The x-axis in Figure 6 is divided into two halves. Peaks to the right of zero represent waves propagating from left to right through the array, and, conversely, peaks to the left of zero designate waves propagating from right to left along the array. Peaks represent maxima when compared to neighboring values in the frequency-wavenumber matrix. Also shown in Figure 6 is the power spectrum measured in the far field.

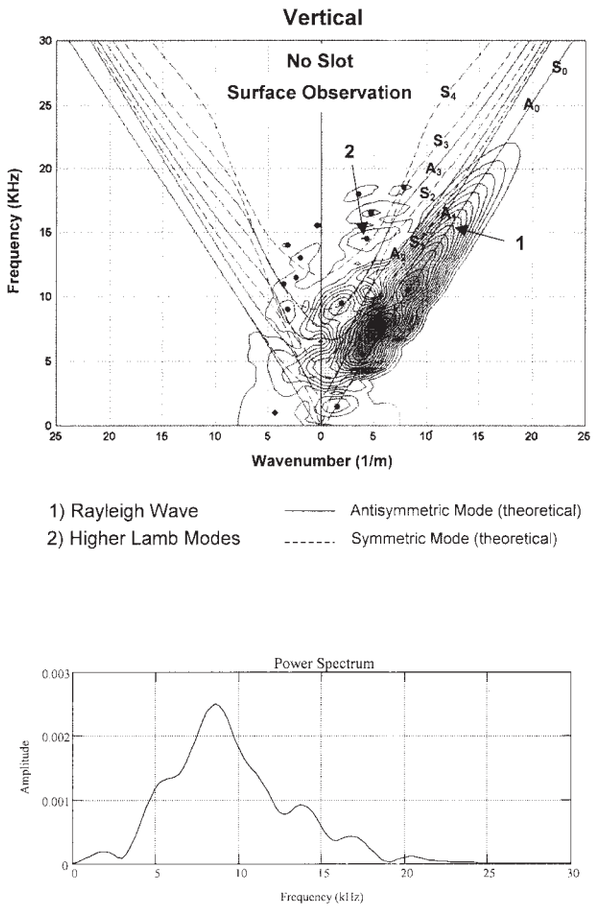

Fig. 6. Frequency-wavenumber plot for finite element nodal accelerations results along the plate surface without a slot.

6. NUMERICAL SIMULATION OF RAYLEIGH WAVE/FRACTURE INTERACTION

The finite element modeling of Rayleigh wave propagation permits gaining unique insight into the interaction between the Rayleigh wave and the slot. In particular, the approach allows gathering data at various depths inside the plate. Conversion of array measurements into the frequency-wavenumber domain allows the examination of the different propagating Lamb modes, including modes that generate the Rayleigh wave. Knowledge of Lamb wave mode shapes and corresponding amplitudes can be used to determine which modes are expected to be measured at specific locations. Differences with anticipated modes provide insight into the Rayleigh wave/fracture interaction.

Three sets of models are examined: no slot, 76.2-mm and 152.4-mm-deep slots. For the three model sets, acceleration histories at 41 nodes behind the slot are recorded at different depths: at the surface, 25.4 mm, 76.2 mm, 127 mm, and 152.4 mm (middle of plate).

6.1. Series I: No Slot

Frequency-wavenumber plots for both vertical and horizontal accelerations at various depths are shown in Figures 7 to 10. Vertical measurements show the presence of a Rayleigh wave up to a depth of 127 mm. In the horizontal orientation, the Rayleigh wave is visible to a maximum depth of 76.2 mm. Short-wavelength Rayleigh wave energy decreases at greater depths. A Rayleigh wave is not observed in the middle of the plate.

The fact that these measurements indicate the presence of a Rayleigh wave is consistent with the concept of a beat wavelength described by Victorov.[6] It occurs because the fundamental modes (A_0 and S_0) are slightly out of phase. According to Victorov, at a distance of half the beat wavelength, the Rayleigh wave has fully migrated to the bottom of the plate. Calculations of half the beat wavelength for the Plexiglas plate

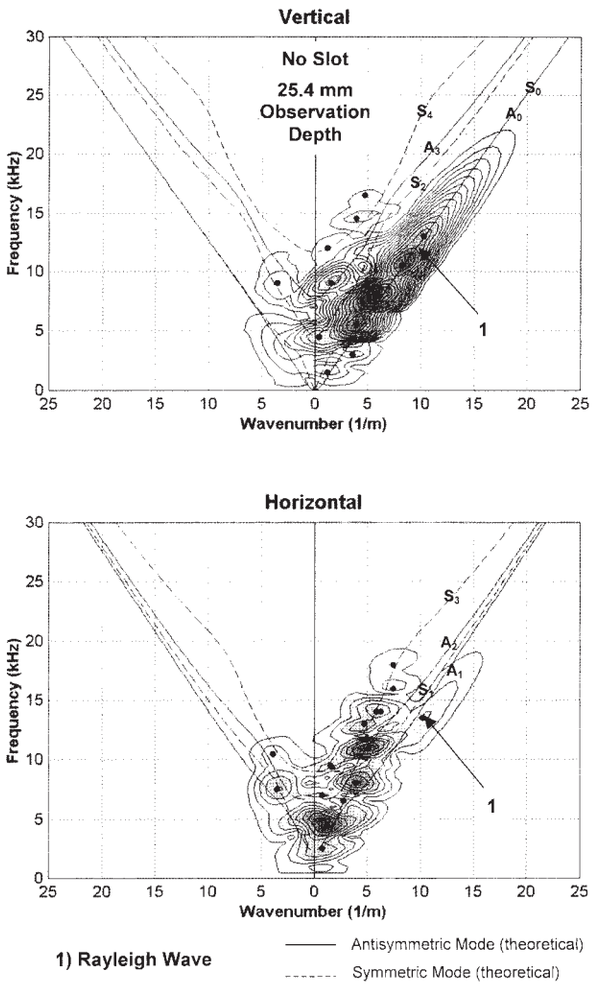

Fig. 7. Frequency-wavenumber plot for vertical and horizontal accelerations without a slot, observed at a depth of 25.4 mm.

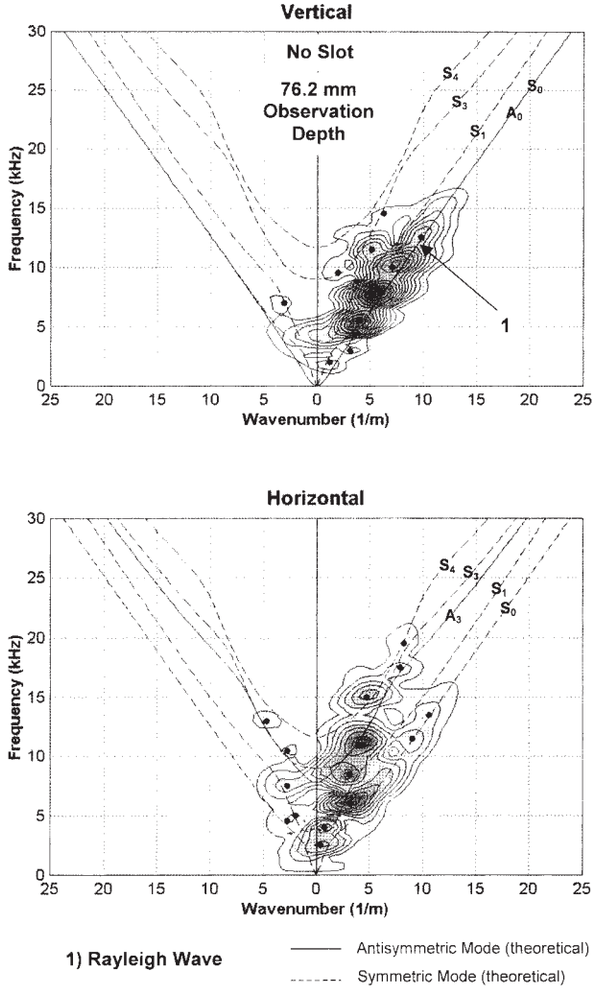

Fig. 8. Frequency-wavenumber plot for vertical and horizontal accelerations without a slot, observed at a depth of 76.2 mm.

used in our investigations is found to be 480 mm from the source for a frequency of about 3.2 kHz and increases to 1.5 m for a frequency of 5 kHz; a distance greater than the plate length. Most of the energy in the presented simulations propagates with frequencies greater than 3.3 kHz, thus we should be able to "see" the Rayleigh wave within the thickness of a plate.

Measurements also reveal higher mode Lamb waves. For comparison and guidance, theoretical dispersion curves calculated using Eq. 1 are superposed onto these plots. The displayed theoretical dispersion curves are chosen to represent high-amplitude modes at specific depths. In determining the high-amplitude modes, mode shapes are calculated using a wavenumber of 3.28 1/m (304.8 mm = plate depth). A smaller value assumes a flexural type motion, whereas a larger value implies pure Rayleigh wave motion. It should be noted that the theoretical calculation of mode shape amplitudes cannot completely explain the observed numerical results. The derivation of the Rayleigh-Lamb frequency equations (Eq. 1), Lamb waves are assumed to be generated by steady-state plane waves while the finite element waveform is transient, resulting in the energy distribution shown in Figure 6. Therefore mode shape calculations using a wavenumber of 3.28 1/m provides a guideline of expected results.

Mode shape amplitudes are normalized with the maximum calculated amplitude for each mode calculated using Eqs. (2), (3), (4), and (5). Tables 1 and 2 list the normalized amplitudes with the highest values

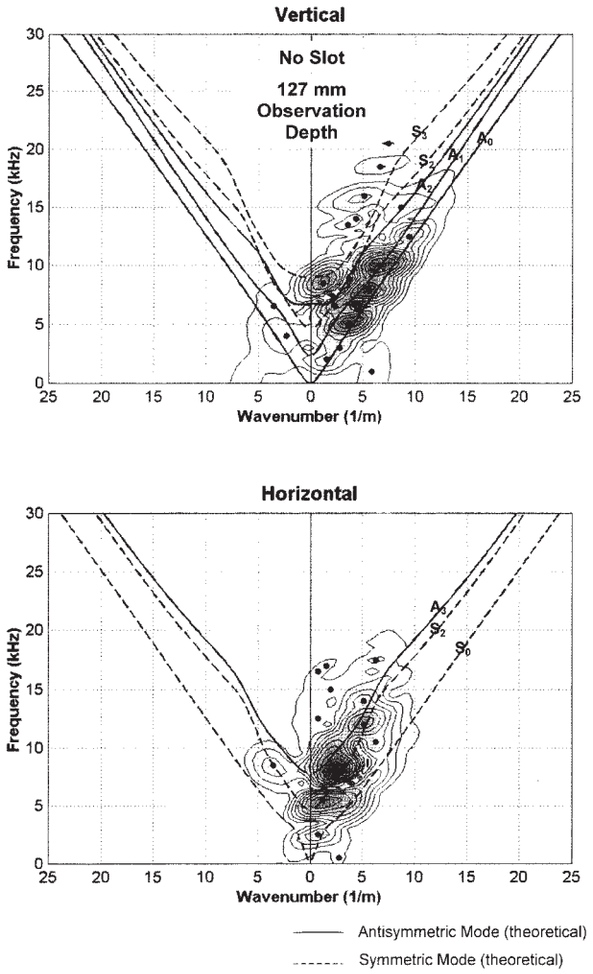

Fig. 9. Frequency-wavenumber plot for vertical and horizontal accelerations without a slot, observed at a depth of 127 mm.

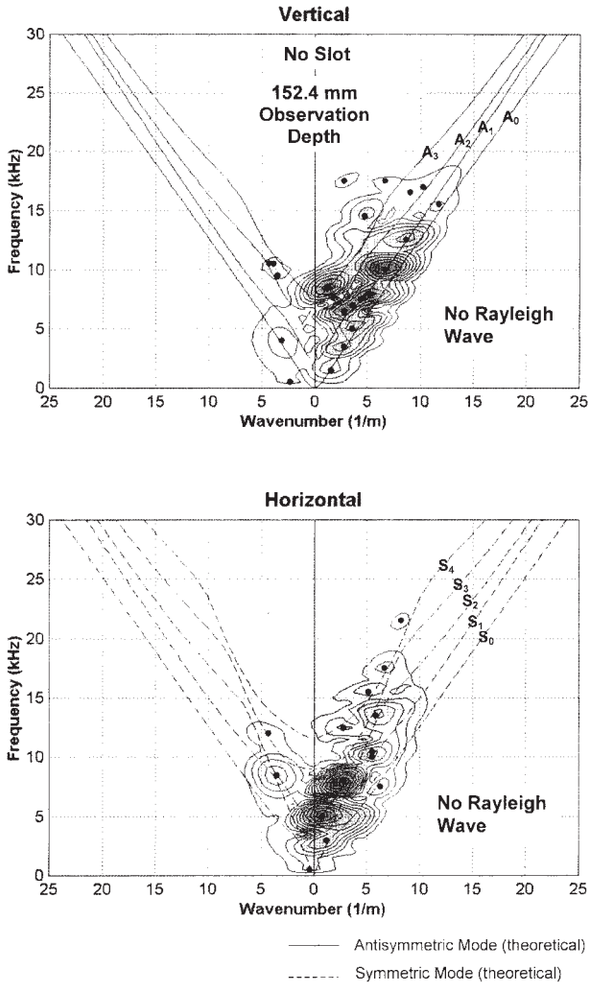

Fig. 10. Frequency-wavenumber plot for vertical and horizontal accelerations without a slot, observed at a depth of 152.4 mm.

Table I. Vertical Motions Normalized with Maximum Amplitude for Each Mode

	Depth (mm)					
Mode	0	25.4	76.2	127	152.4	304.8
S_0	0.969*	0.991*	0.726*	0.265	0	0.969*
S_1	1*	0.506	0.618*	0.526	0	1*
S_2	0.966*	0.784*	0.481	0.595*	0	0.966*
S_3	0.377	0.064	0.575*	0.796*	0	0.377
S_4	0.984*	0.651*	0.979*	0.257	0	0.984*
A_0	0.945*	1*	0.923*	0.835*	0.822*	0.945*
A_1	0.265	0.14	0.464	0.922*	1*	0.265
A_2	0.277	0.064	0.057	0.807*	1*	0.277
A_3	0.994*	0.766*	0.475	0.405	0.252*	0.994*

* Modes graphed in subsequent frequency-wavenumber plots.

Table II. Horizontal Motions Normalized with Maximum Amplitude for Each Mode

	Depth (mm)					
Mode	0	25.4	76.2	127	152.4	304.8
S_0	1*	0.287	0.445*	0.714*	0.744*	1*
S_1	0.806*	0.985*	0.718*	0.066	0.059	0.806*
S_2	0.223	0.286	0.298	0.766*	1*	0.223
S_3	0.995*	0.677*	0.703*	0.09	0.213	0.995*
S_4	0.596	0.046	0.433*	0.356	1*	0.596
A_0	1*	0.428	0.008	0.029	0	1*
A_1	1*	0.475*	0.106	0.121	0	1*
A_2	0.993*	0.895*	0.1	0.197	0	0.993*
A_3	0.384	0.053	0.421*	0.831*	0	0.384

* Modes graphed in subsequent frequency-wavenumber plots.

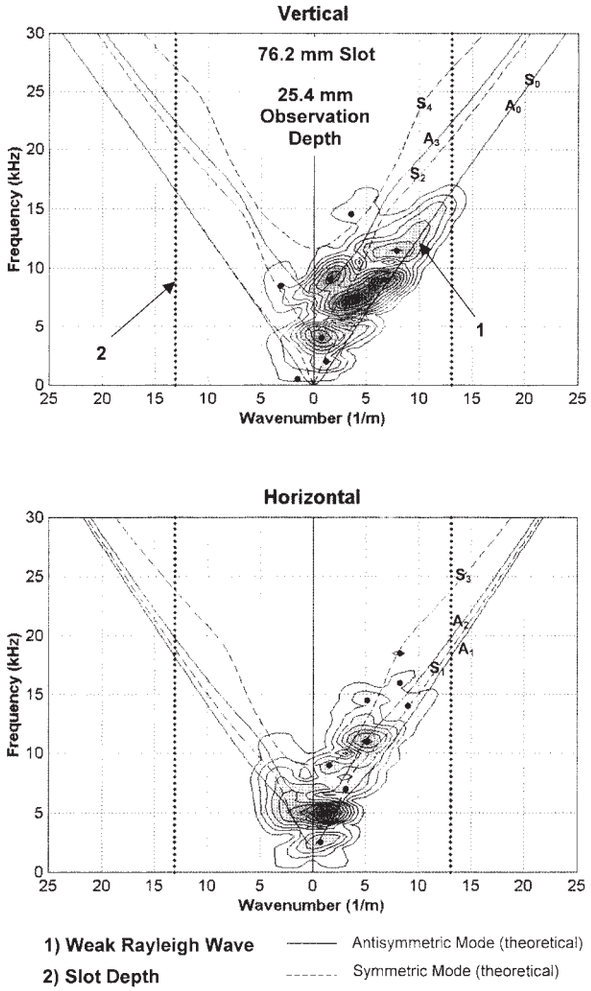

Fig. 11. Frequency-wavenumber plot for vertical and horizontal accelerations with a 76.2-mm slot, observed at a depth of 25.4 mm.

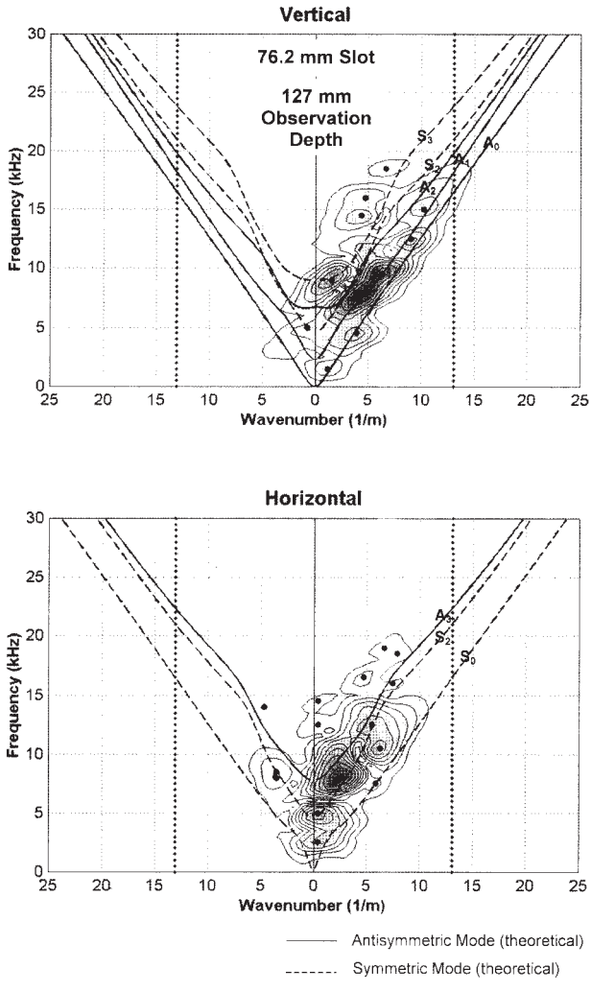

Fig. 12. Frequency-wavenumber plot for vertical and horizontal accelerations with a 76.2-mm slot, observed at a depth of 127 mm.

shown on the frequency-wavenumber plots. Values range between 0 and 1, where 1 represents the ability to easily observe a particular mode at a certain depth.

The theoretical dispersion curves plotted in Figures 7 to 10 show very good agreement with numerically predicted vertical and horizontal motions. In particular, the numerical horizontal motions of all flexural modes, and vertical motions of all symmetric modes, are equal to zero in the middle of the plate.

6.2. Series II: 76.2-mm Slot

Figures 11 and 13 show frequency-wavenumber plots for simulations of the plate with a 76.2-mm-deep slot. The vertical dotted line represents the slot depth as a wavenumber. Fewer Rayleigh wave peaks are observed because a smaller number of receivers record the reformed Rayleigh wave. Vertically oriented motions indicate the maximum Rayleigh wave depth is 76.2 mm.

Vertical motions of Lamb modes show a partial agreement with anticipated high-amplitude dispersion curves up to a depth of 76.2 mm. The agreement is better for horizontal motions. For the 127-mm (Fig. 12) and 152.4-mm observation (Fig. 13) depths, measurements are identical to those made without a slot. Plotted theoretical dispersion curves correspond to high amplitude modes examined in Series I.

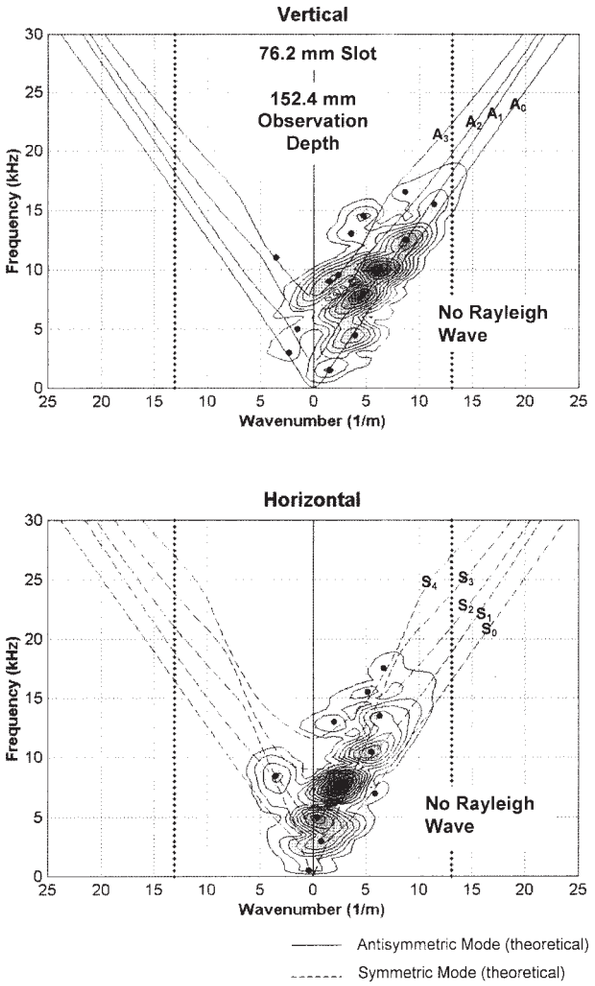

Fig. 13. Frequency-wavenumber plot for vertical and horizontal accelerations with a 76.2-mm slot, observed at a depth of 152.4 mm.

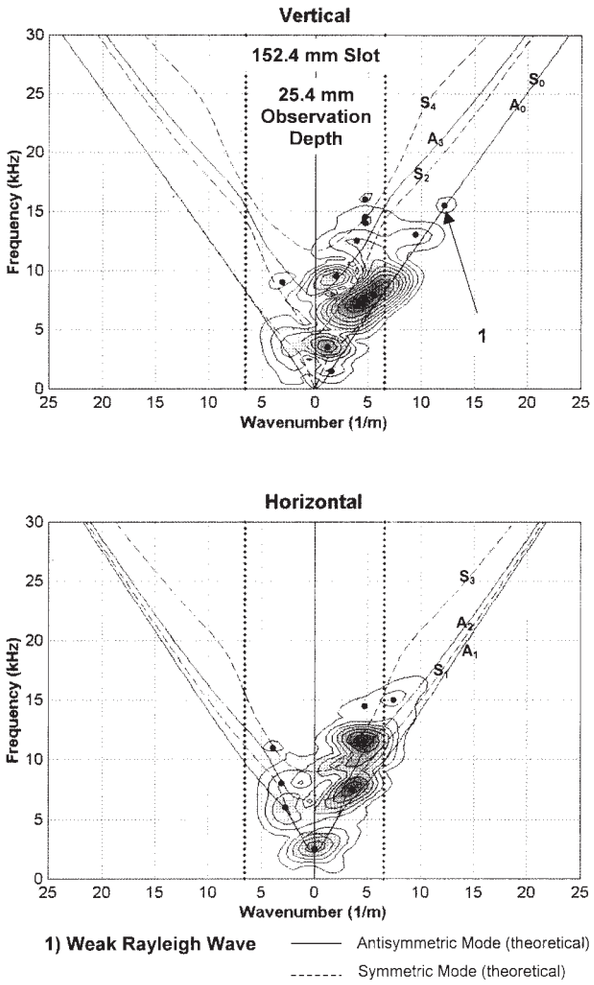

Fig. 14. Frequency-wavenumber plot for vertical and horizontal accelerations with a 152.4 mm slot, observed at a depth of 25.4 mm.

6.3. Series III: 152.4-mm Slot

Increasing the slot depth to 152.4 mm weakens the Rayleigh wave. Figures 14 and 16 show frequency-wavenumber plots for nodal observations at depths of 25.4, 127, and 152.4 mm. The maximum depth of vertical Rayleigh wave motion is 76.2 mm. However, this Rayleigh wave differs from the Rayleigh wave observed in Series I or II. The Rayleigh wave in Series III has only one or two peaks at wavelengths shorter than the slot depth. Numerically recorded horizontal motions do not reveal any Rayleigh wave motion.

High-amplitude vertical and horizontal motions of Lamb modes only partially agree with the theoretical dispersion curves up to a depth of 127 mm. At a depth of 152.4 mm the results are quite close to the numerical observations made in Series I and II.

DISCUSSION AND CONCLUSIONS

In summary, Series I results show that high-amplitude Lamb modes are in agreement with simulated results and ideal plate theory. Series II and III results show poor agreement with ideal plate theory at depths (h) less than the slot depth (d) (when $h/d < 1$), whereas very good agreement is obtained at depths greater than or equal to the slot depth (when $h/d \geq (1)$.

These results show that the presence of a surface discontinuity or slot effectively blocks shorter-wave-

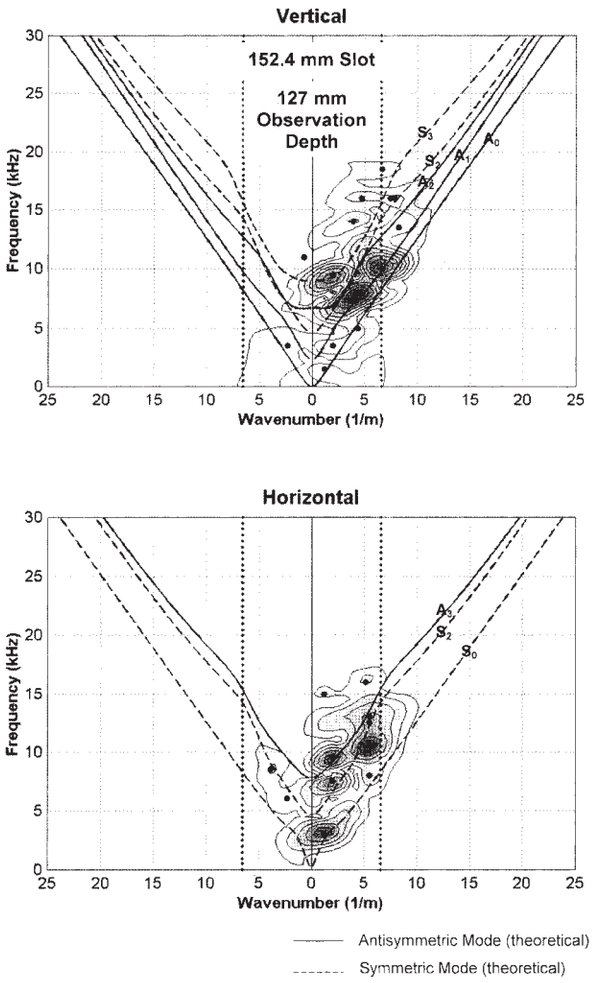

Fig. 15. Frequency-wavenumber plot for vertical and horizontal accelerations with a 152.4-mm slot, observed at a depth of 127 mm.

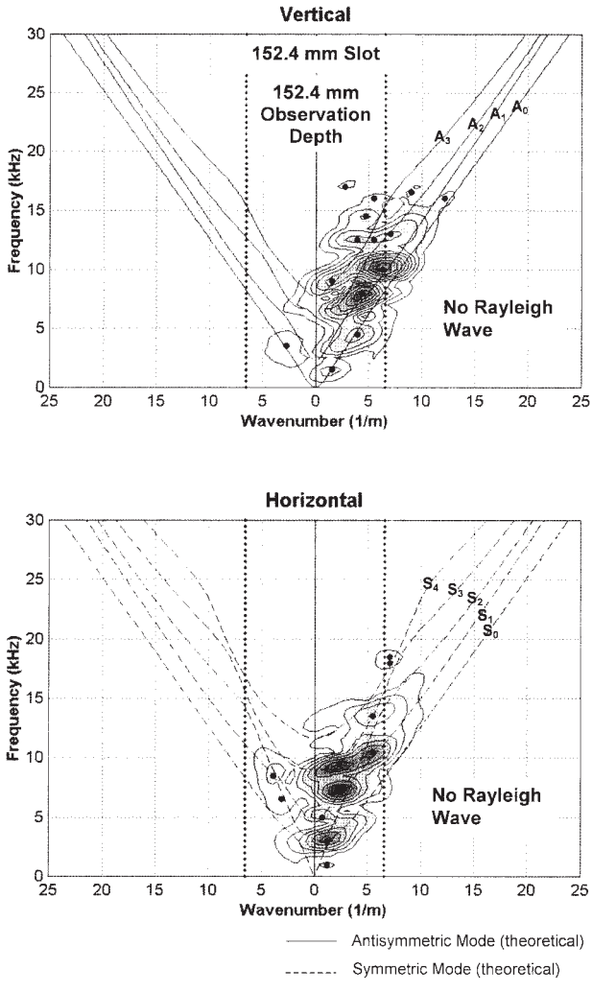

Fig. 16. Frequency-wavenumber plot for vertical and horizontal accelerations with a 152.4-mm slot, observed at a depth of 152.4-mm.

length Rayleigh waves, allowing longer wavelengths to pass. Although longer wavelengths pass the slot, energy redistribution will occur at some distance behind the slot. The slot essentially breaks the transient motion, so that wave propagation behind the slot encompasses long wavelengths passing the slot and mode converted short-wavelength energy. Both types of motion are combined in the above frequency-wavenumber plots. The various types of motion are likely affected by array location, which is not addressed in this study.

Numerical results without a slot indicate the presence of a strong Rayleigh wave. As the slot depth increases compared to the plate depth (t) (d/t = (0.25), the Rayleigh wave becomes weaker but remains intact. The Rayleigh wave observed behind deep slots (d/t = 0.5) is weak and shows only partial resemblance with the original Rayleigh wave. In Series II the Rayleigh wave is formed by long-wavelength energy passing the slot, whereas the Rayleigh wave in Series III is formed by mode converted Lamb modes. The vector plots shown in Figures 17 and 18 clearly illustrate these observations. These results are consistent with numerical measurement predictictions made by Alleyne and Cawley.[29] In their study, individual fundamental Lamb modes impinging on a fracture generated both types of fundamental modes behind the fracture.

In summary, numerical simulation results not only confirm experimental measurements but also provide unique information at locations that are experimentally unreachable. This type of detailed information facilitates understanding the effect of surface anomalies and discontinuities on the propagation of Rayleigh waves.

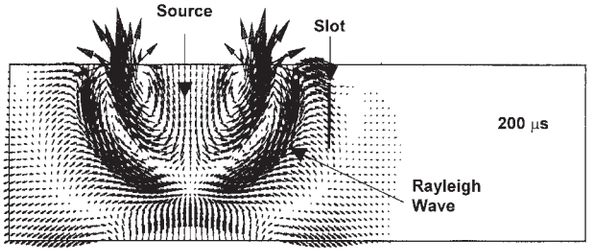

Fig. 17. Vector plot of nodal accelerations at 200 μs. Plate with a 76.2-mm slot depth.

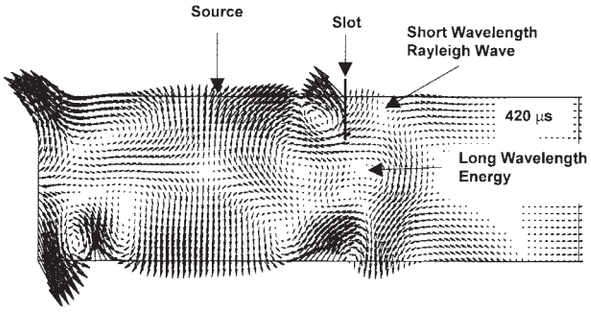

Fig. 18. Vector plot of nodal accelerations at 420 μs. Plate with a 76.2-mm slot depth.

Results show that anomalies act as low-pass filters. The Rayleigh wave measured behind the slot comprises two components: one related to the Rayleigh wave generated in front of the slot and another formed because of the slot. The depth of discontinuities can be inferred from the frequencies that are filtered.

ACKNOWLEDGMENTS

This research was supported by the Natural Sciences and Engineering Research Council of Canada (NSERC).

REFERENCES

1. L. L. Morgan, "The spectroscopic determination of surface topography using acoustic surface waves." *Acustica* **30,** 222–228 (1974).
2. J. D. Achenbach, A. K. Gautesan and H. McMaken, "Application of elstodynamic ray theory to diffraction by cracks," in *Modern Problems in Elastic Wave Propagation*, edited by J. Miklowitz and J. D. Achenbach. International Union of Theoretical and Applied Mechanics, pp. 219–237 (1977).
3. M. G. Silk, "The determination of crack penetration using ultrasonic surface surface waves", Ultrasonics, **38,** pp. 290–297 (1976).
4. M. Sansalone and M. J. Carino, "Detecting Delaminations in Concrete Slabs with and without Overlays Using Impact Echo Method," *J. Am. Concrete Instit.* **86,** pp. 175–184 (1989).
5. M. Hirao, K. Tojo and H. Fukuoka, "Spectrum Analysis for Rayleigh Waves Reflected from Small Fatigue Cracks," *Nondestruct. Test. Eval.* **7,** pp. 223–232 (1992).
6. I. Victorov, *Rayleigh and Lamb Waves: Physical Theory and Applications* 1967, Plenum Press, New York.
7. B. R. Tittmann, F. Cohen-Ténouodji, M. De Billy, A. Jungman and G. Quentin, "A Simple Approach to Estimate the Size of Small Surface Cracks with the Use of Acoustic Surface Waves," *Appl. Physics Lett.* **33,** pp. 6–8 (1978).
8. V. Domarkus, B. T. Khuri-Yakub and G. S. Kino, "Length and Depth Resonances of Surface Cracks and Their Use for Crack Size Estimation," *Appl. Physics Lett.* **33,** pp. 557–559 (1978).
9. B. R., Tittmann, O. Buck, G. Ahlberg, M. De Billy, F. Cohen-Ténouodji, A. Jungman and G. Quentm, "Surface Wave Scattering from Elliptical Cracks for Failure Prediction," *J. Appl. Physics* **51,** pp. 142–150 (1980).
10. C. H. Yew, K. G. Chen and D. L. Wang, "An Experimental Study of Interaction Between Surface Waves and Surface Breaking Crack," *J. Acoust. Soc. Am.* **75,** pp. 189–196 (1984).
11. M. Picornell and R. L. Lytton, "Field Measurement of Shrinkage Crack Depth in Expansive Soils," *Transport. Res. Rec.* **1219,** pp. 121–130 (1989).
12. M. E. Kalinski, K. H. Stokoe II, J. O. Jirsa and J. M. Roësset, "Nondestructive Identification of Internally Damaged Areas on a Concrete Beam Using the Spectral Analysis of Surface Wave Method," *Transport. Res. Rec.* **1458,** pp. 14–19 (1994).
13. A. Zerwer, "Near Surface Fracture Detection in Structural Elements: Investigation Using Rayleigh Waves," Ph.D. Dissertation, University of Waterloo, Ontario, Canada, pp. 368.
14. A. Zerwer, M. A. Polak, J. C. Santamarina, "Experimental Investigation of Wave Propagation in Thin Plexiglas Plates: Implications for Modeling and Measuring Rayleigh Waves," *NDT&E Int.* **33,** pp. 33–41 (2000).
15. A. Zerwer, M. A. Polak, J. C. Santamarina, "Fracture Detection in Concrete Using Rayleigh Waves," submitted to *NDT&E Int.* (2000).
16. A. Zerwer, M. A. Polak, J. C. Santamarina, "The Effects of Surface Cracks on Rayleigh Wave Propagation: An Experimental Study," *ASCE J. Struct. Eng.* **128,** pp. 240–248 (2001).
17. L. Rayleigh, "On Waves Propagated Along the Plane Surface of an Elastic Solid," *Proc. Lond. Math. Soc.* **17,** pp. 4–11 (1885).
18. H. Lamb, "On Waves in an Elastic Plate," *Proc. Lond. Math. Soc.* **21,** pp. 85–95 (1889).
19. J. Oliver, "Elastic Wave Dispersion in a Cylindrical Rod by Wide-Band Short-Duration Pulse Technique," *J. Acoust. Soc. Am.* **29,** pp. 189–194 (1957).
20. K. F. Graff, *Wave Motion in Elastic Solids*, 1975, Dover Publications, New York.
21. H. S. Valliappan and V. Murti, "Finite Element Constraints in the Analysis of Wave Propagation Problems," UNICIV Rep. No. R-218, Oct. 1984, The University of New South Wales, The School of Civil Engineering.
22. M. Liu and D. G. Gorman, "Formulations of Rayleigh Damping and Its Extensions," *Comput. Struct.* **57,** pp. 277–285 (1995).
23. J. Koppelmann, "Uber die Bestimmung des dynamischen Elastizitätsmoduls und des dynamischen Schubmoduls im Frequenzbereich von 10–5 bis 10–1 Hz," *Rheol. Acta* **1,** pp. 20–28 (1958).
24. S. C. Hunter, "Energy Absorbed by Elastic Waves During Impact," *J. Mechan. Physics Solids* **5,** pp. 162–171 (1957).
25. T. M. Proctor Jr. and F. R. Breckenridge, "Source Force Waveforms: The Use of a Calibrated Transducer in Obtaining an Accurate Waveform of a Source," *J. Acoust. Emission* **10,** pp. 43–48 (1992).

26. J. A. Zukas, T. Nicholas, H. F. Swift, L. B. Greszczuk and D. R. Curran, *Impact dynamics*, 1982, John Wiley and Sons.
27. L. G. Peardon, "FK Techniques in Seismic Processing," in *Geophysical Signal Processing*, edited by E. A. Robinson and T. S. Durrani, pp. 388–474, Prentice Hall, Englewood Cliffs, NJ.
28. D. N. Alleyne and P. Cawley, "A Two-Dimensional Fourier Transform Method for the Measurement of Multimode Signals," *J. Acoust. Soc. Am.* **89,** pp. 1159–1168 (1991).
29. D. N. Alleyne and P. Cawley, "The Interaction of Lamb Waves with Defects," *IEEE Trans. Ultrason. Ferroelectr. Frequency Control* **39,** pp. 381–397 (1992).